ORIGINAL PAPER

Active morphogenic faulting and paleostress analyses from the central Nahan Salient, NW Siwalik Himalaya

Ajay Kumar[1] · Mohamedharoon A. Shaikh[2] · Sarabjeet Singh[1,3] · Tejpal Singh[3] · Soumyajit Mukherjee[2] · Seema Singh[1]

Abstract

Tectonics of ancient foreland basins of collisional orogens are of enormous international attention from the perspectives of applied (e.g., hydrocarbon exploration) and theoretical geosciences (e.g., tectonic models). Morphogenic faulting produces identifiable surface morphology and structural patterns that provide vital insights for reconstructing paleostress scenarios and the present-day surface topography. The principal stress directions that affected the region are important to understand the polyphase tectonic zones. We perform geomorphic analyses and combine them with paleostress analysis of mesostructures from the Panchkula-Morni region from the central Nahan Salient. We reconstruct the orientation of the principal stress axes that evolved during the tectonic evolution of the brittle sheared sandstones of the Lower/Upper Siwalik units. Three deformation phases are determined that are interpreted to be coeval with the Himalayan orogeny: *(i)* extensional stress field with NW oriented extension, (ii) extensional stress field with NE–ENE oriented extension, and (iii) NE-directed compression. Out of these, component (iii) led to the uplift of the Himalayan orogen and produced the present-day topography. Slickenside kinematic indicators viz., PT, RM and PO structures helped in interpreting the movement of the slip planes exposed in the uniform lithology. Compressional stress field with NE compression is consistent with the geometry of the Bisiankanet Thrust (BkT) inferred from geomorphic analyses. The NE extension direction and oblique plunge of the σ_1-axis may be responsible for the oblique movement with major normal slip at the western extremity of the BkT. Abrupt change in topographic swath profiles, their mutual offset in the hangingwall and knickpoint migration indicate active uplift especially across the newly identified out-of-sequence Tikkar Tal Thrust (TTT) on the map and also on an existing seismic section.

Keywords Deformation mechanism · Collisional tectonics · Destructive plate margin · Physical geology · Surface topography · Active fault

Introduction

While discussing the importance of fold and thrust belts for hydrocarbon geosciences worldwide, Goffey et al. (2010) opined that more geological and structural data are required

✉ Tejpal Singh
  tejpal@csio.res.in; geotejpal@yahoo.co.in

✉ Soumyajit Mukherjee
  soumyajitm@gmail.com; smukherjee@iitb.ac.in

1 Department of Geology, Panjab University, Chandigarh 160014, India

2 Department of Earth Sciences, Indian Institute of Technology Bombay, Powai, Mumbai, Maharashtra 400 076, India

3 CSIR-Central Scientific Instruments Organisation, Chandigarh 160030, India

from such regions to get a clearer picture for exploration (also see Cooper 2007). Hammerstein et al. (2020) pointed out that the lack of quality 3D seismic imaging from such terrains remains the number one problem in detail subsurface structural analyses.

In 1960s, the Oil and Natural Gas Commission (ONGC) studied the Himalayas from the perspective of hydrocarbon exploration (Karunakaran and Ranga Rao 1979; Raiverman et al. 1994). Only limited success was achieved mainly as gas discovery from the Siwalik range (review in Mishra and Mulhopadhyay 2012). Siwalik and Lesser Himalayan zones together have been described structurally as a fold and thrust belt, where structural data from the Siwalik region has still remained scanty (Mishra and Mulhopadhyay 2012). Hydrocarbon companies (e.g., Rao 1986) have continued investigation in the Himalayas. Dutta and Samanta (2008) performed

thermal modelling and cross-section balancing from this region. These authors reported that the Subathu and Lower Dharamsala formations are mostly thermally mature. In this context, targeting mega structures in the Siwalik range is needed more intensely.

So far several wells have been drilled in the Siwalik region of Punjab and the nearby areas but no economic success has been attained. However, the chance is certainly not zero since (i) the basal Dharamsala unit around 5499–6715 m depth demonstrated moderately good residual organic richness (average TOC > 1%, HI > 153; Dutta and Samanta 2008); (ii) several oil and gas shows have been documented through drilling operations (reviewed in Table 1 in Craig et al. 2018), and specifically from the Nahan area (reviewed in Table 1 in Mishra and Mukhopadhyay 2012); (iii) in the adjacent region of Siwalik in Punjab, from Jammu area a good indication of hydrocarbon has been obtained more than ten years back (Sharma 2015); (iv) the nearby Jwalamukhi area in the Siwalik Indian Himalaya has been emitting gas since time immemorial leading to think that there has been "gas pool"/"excellent potential reservoirs" in the Lower Siwalik rocks (e.g., Mittal et al. 2006; Craig et al. 2018); and (v) the presence of good to excellent quality potential reservoirs.

Morphogenic faulting produces identifiable surface topographic markers and patterns that can be easily seen on space-based imageries (Caputo 2005; Walker 2006; Vakaet al. 2020; Gill et al. 2021). The spatial distribution of these markers and patterns is primarily controlled by the lithologic contrasts and variation in tectonic and/or climatic patterns. In areas of near-uniform climate such as the western sub-Himalaya of India (e.g., Singh et al. 2009, 2021), lithology
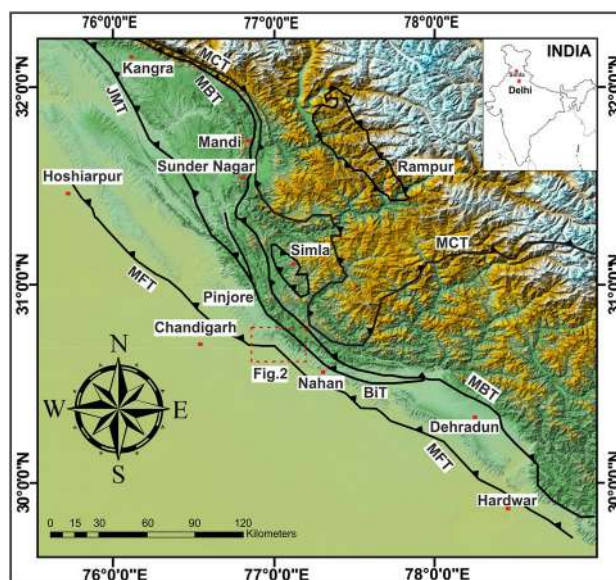

Fig. 1 Map showing the distribution of surface topography of the Indian western Himalaya that clearly displays segmentation of the Sub(Outer)-Himalaya along its strike in the Kangra Reentrant-Nahan Salient-Dehradun Reentrant (Singh et al. 2012). The main geological structures are: main central thrust (MCT), main boundary thrust (MBT) and main frontal thrust (MFT). Other structures include Jwalamukhi Thrust (JMT) and Bilaspur thrust (BiT). Red dotted polygon: study area in Fig. 2. Trace of MBT in other sections of western Himalaya can be found in Bose and Mukherjee (2020)

acts as a dominant control principally driven by tectonics along with spatially and temporally varying stress trajectories (Sperner and Zweigel 2010; Shaikh et al. 2020, Maurya et al. 2021).

Table 1 Stratigraphy of the Nahan Salient (from Raiverman et al. 2002; Singh and Virdi 2007)

|	Division	Formation	Age
Post-Siwalik Deposits		Alluvium/piedmont	Recent to Late Pleistocene
		Unconformity	
		Terrace deposits	Early late Pleistocene
		Unconformity	
Siwalik Group Deposits	Upper Siwalik	Boulder conglomerate	Late Pliocene
		Pinjore	Middle Pliocene
		Tatrot	Middle Pliocene
		Tectonic contact	
	Middle Siwalik	Dhokpathan	Early Pliocene
		Nagri	Late Miocene
	Lower Siwalik	Chinji	Middle Miocene
		Kamlial	Early Miocene
		Tectonic contact	
Pre-Siwalik deposits		Kasauli	Early late Oligocene
		Dagshai	Late Palaeocene-
		Subathu	Middle Eocene
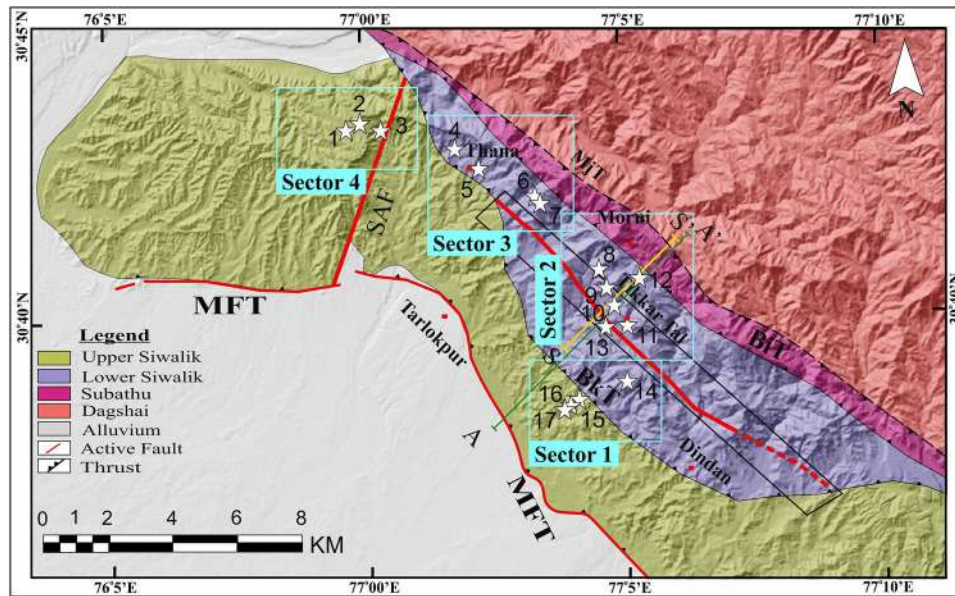
Fig. 2 Detailed geologic map of the study area (adopted from Geological Survey of India) showing Main Frontal Thrust (MFT), Bisiankanet Thrust (BkT) which is locally also known as the Nahan Thrust and Bilaspur Thrust (BiT). The Sabilpur Active Fault (Gill et al. 2021) and the newly identified TTT is shown in red. Black rectangle: tentative location of Fig. 8 that encloses the new active fault shown in red. Based on field structural data, the study area is divided into four sectors which are marked by blue boxes and labelled accordingly. The white stars show the location of sites 1–17 which are discussed in the text. Green line (A–A′): location of the swath profile shown in Fig. 3. Yellow line: seismic section in Fig. 10

In this study, we focus on an internal thrust sheet of the Bisiankanet Thrust (BkT), locally also known as the Nahan Thrust (Singh and Virdi 2007; Singh et al. 2007). The BkT presents a curved map trace that joins the Bilaspur Thrust (BiT) on either extreme to the west and east (Figs. 1, 2). The topography of the BkT sheet also varies; it is elevated and has high relief closer to the thrust front whereas it has low elevation and relief within the thrust sheet (Figs. 1, 2). Such variable geomorphology mandates for integrating the tectono-geomorphic investigations with paleostress analyses to deduce the ingrained structural and tectonic controls.

Paleostress analysis is a commonly used technique in structural geology (Doblas et al. 1997; Sperner and Zweigel 2010). It characterizes the stress systems that have been functioning in the past and explains the multiple tectonic events from their record in deformation structures, most commonly from fault-slip data (Simón 2019). The output of paleostress analysis is a reduced stress tensor that includes the orientations of the three mutually perpendicular principal stress axes, viz. the maximum, intermediate and minimum principal stress axes (σ_1, σ_2 and σ_3, respectively); and the stress ratio [$R = (\sigma_2 - \sigma_3)(\sigma_1 - \sigma_3)^{-1}$] define the shape of stress ellipsoid (Angelier 1994; Vanik et al. 2018; Dutta et al. 2019; Maurya et al. 2021; Shaikh et al. 2020; Goswami et al. 2022). One can also obtain the orientations of the maximum and minimum horizontal principal stress (S_{Hmax} and S_{Hmin}).

The presented work from the Sub-Himalayan ranges of NW India identifies surface faulting based on (i) geomorphic phenomenon and morphometric analyses, and (ii) field observations and (paleo)stress analysis. Detailed field investigations reveal the kinematics of faulting and involved (paleo)stress conditions. Fault slip data were collected from in-situ rock exposures. The study emphasizes the need to integrate kinematic information with remote sensing observations to justify the tectonic origins and surface manifestations of the morphogenic faulting.

Geology

The Sub-Himalayan belt is located between the outermost Main Frontal Thrust (MFT) and the internal Main Boundary Thrust (MBT). Several internal thrusts between the MFT and MBT cut across the sub-Himalayan ranges and are supposedly active (Singh and Virdi 2007; Singh et al. 2007, 2012, 2014; Singh and Awasthi 2010, 2019; Mukherjee 2015; Dey et al. 2016; Kaushal et al. 2017). The activity along the MFT has recently been interpreted from this region of the Nahan salient (Thakur et al. 2021).

Broadly, the NW sub-Himalaya is laterally divided into the two structural re-entrants formed by the curved trace of MBT, viz., Kangra (towards west) and Dehradun (towards east). The reentrants are interposed by the Nahan Salient (Fig. 1). The dimension of the Nahan salient between the Ghaggar river till the Markanda river is ~ 40 km. Topography, relief and tectonic deformation varies significantly along-strike within the salient from west to east (Singh and Virdi 2007; Singh and Awasthi 2010; Singh et al. 2011, 2014; Kaushal et al. 2017). In the west, just east of the Ghaggar river the MFT is marked by a small topographic ridge of the Nadah Anticline in its hangingwall (an extension of the Chandigarh anticline). Towards the east and in the central part of the Nahan salient, the MFT is characterized by a subdued fold topography in the hanging wall of the MFT. This part is also characterized by wavering trace of the Bisiankanet Thrust (BkT, locally known as Nahan Thrust). Further east, the topography is more subdued and marked with wider channels depositing broad terraces (Fig. 2). The BkT generally strikes NW–SE, almost sub-parallel to the MFT but it wavers on either side to cut up-section, giving rise to lateral ramps on either side, which join the Bilaspur Thrust (BiT) towards the north. The BkT is not exposed in the narrow region perhaps due to its geometry and consequent joining with the BiT in the sub-surface. The change in the geometry of the BkT corresponds with a prominent topographic scarp within its thrust sheet in the central part of the Nahan salient, where the thrust curves and the thrust sheet are widest. This scarp is located within 5 km of the MFT (Figs. 1, 2).

The BkT sheet is bound to the north by the BiT that brings the Lower Tertiary rocks over the Siwalik rocks. The Lower Siwalik is thrust over the Upper Siwalik along the BkT. Table 1 presents the stratigraphy of the area. Our investigation is focused on the BkT in the central part of the Nahan salient.

Geomorphologic studies

We study the morphologic signatures of the Nahan salient, which displays a prominent scarp in the central part (Fig. 2). The typical linear surface trace was picked up on topographic maps and DEM, while it was not readily visible on the satellite images, perhaps due to vegetation (Fig. 2). The scarp is south-facing and has been analysed using topographic swath profiles drawn along and across the Sub-Himalayan belt in the central part of the Nahan salient (Figs. 3, 4). The profiles include minimum, maximum and mean elevations across a swath width of 1 km and they capture a generalized view of topographic relief distribution across the profile line. Swaths make it more reasonable and consistent for drawing inferences about the tectonics from topography. In addition, the basins within the scarp bear a typical wine-glass shape (Supplementary Fig. S1; see Miccadei et al. 2013 for use of the term "wine-glass shape). All these features suggest active faulting and concomitant uplift, which has been investigated further in detail.

In particular, to examine the impact of active faulting on stream network we have used the Normalized Steepness (K_{sn}) index. The index has been widely used as a reliable proxy to detect tectonically-induced perturbations in river longitudinal profiles (Kirby and Whipple 2012; Jaiswara et al. 2020). It consistently exhibits a good direct spatial relationship with uplift/erosion rates obtained from geomorphic metrices that are consistent with other sophisticated methods such as cosmogenic radionuclide (CRN) dating (Wobus et al. 2006; Kirby and Whipple 2012; Dey et al. 2016). A derivative of the simple longitudinal profile (Singh and Awasthi 2010), the calculation presumes an equilibrium state stream gradient defined by a power-law scaling between the slope (S) and the contributing drainage area (A).

$$S = k_s A^{-\theta}. \tag{1}$$

Here k_s is the channel steepness index, and θ is the concavity index. There could be large variations in channel steepness

Fig. 3 Swath elevation profile across A–A′, shown in Fig. 2. Black line: mean elevation bound by swath edges showing minimum (bottom) and maximum (top) elevations at the same point. Red line: local relief. Existing structures are marked along with the profile. TTT, identified in this study, is also shown
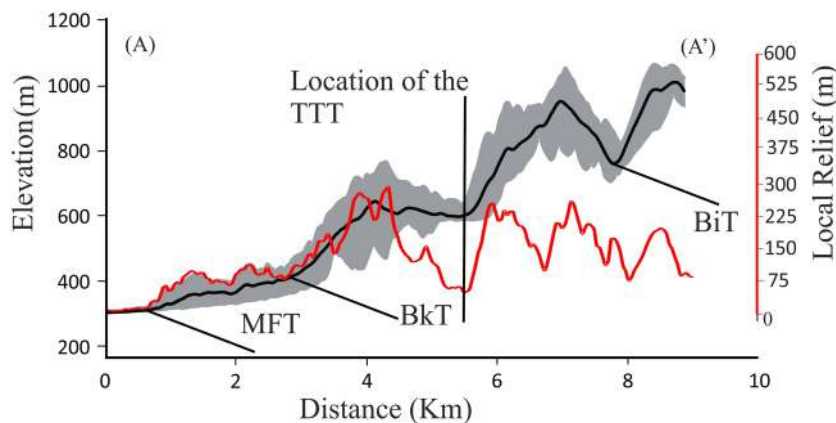
Fig. 4 The top panel shows the swath elevation profiles in the hangingwall (grey) and footwall (red) along with the TTT. A clear decrease in elevations can be seen. The bottom panel shows local relief along the same two transects show a sharp increase in relied upon the actively uplifting hanging wall. Light pink box: most pronounced zone of active faulting with maximum elevation and relief contrast
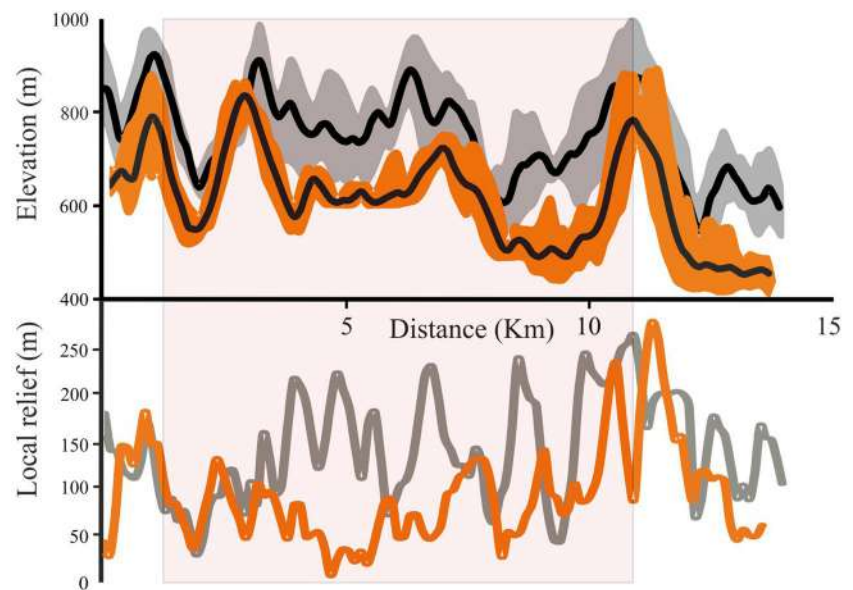
due to small uncertainties in the concavity thereby making it redundant for comparison across basins of varying shapes and sizes (Wobus et al. 2006). Therefore, normalization of the steepness index with a reference concavity (θ_{ref}) allows a more robust measure to compare across basin shapes and sizes, which is known as the normalized channel steepness (k_{sn}) index:

$$S = k_{sn}A^{-\theta_{ref}}, \tag{2}$$

Here the reference concavity ranges $0.4 \leq \theta \leq 0.6$ for steady-state channels (e.g., Wobus et al. 2006; Jaiswara et al. 2020).We have considered $\theta_{ref} = 0.45$.

Accordingly, an increase in rock uplift rate would enable the stream to incise faster in response. This is typically achieved by steepening its bed and narrowing its width. As a consequence, there is an increase in channel gradient "knickpoint" first in the downstream reach of the higher uplift zone which subsequently migrates upstream. The knickpoint separates adjusted, steeper (high k_{sn}) reaches from unadjusted, "relict" (lower k_{sn}) reaches (Whipple and Tucker 1999). Areas of higher rock uplift are characterized by higher k_{sn} values.

Structural geology

Structural/paleostress investigations

Meso-scale brittle structural investigations were carried out to explain the dynamic evolution of the study area. The study area exposes Lower Siwalik calcareous sandstones. We chose 17 well-exposed data sites. The outcrops usually have good 3D exposures and a significant number of striated faults. We measured a total of 246 polyphase fault-slip data and noted the slip-sense.

Polyphase fault-slip data including complete and incomplete fault-slip data were collected. Fault-slip data including the attitude of the fault plane and associated slickenside lineations provides a complete datum and are therefore referred to as complete fault-slip information (Yamaji and Sato 2019; Shaikh et al. 2020). Fault-slip data with insufficient information are called *incomplete* (Yamaji and Sato 2019; Shaikh et al. 2020). Data without the information of fault slip-sense are called *line-only data* (Sato 2006; Yamaji and Sato 2019). Data without the information of fault slip direction are called *sense-only data* (Yamaji and Sato 2019).

We examined fault-slip data with reliable kinematic indicators, such as striations with concomitant fractures and mineral growth fibers. A confidence level was attributed to the observed kinematics on each fault-slip measurement, according to Sperner and Zweigel (2010): 1—certain, 2—unreliable and 3—unknown. The fault-slip data with a certain confidence level include complete fault-slip datum. Incomplete fault-slip data came into the other two categories. Unreliable data was defined as faults with indeterminate slip-sense (or line-only data). Faults lacking slip-sense and slip direction information were classified as unknown fault-slip data. During data analysis, we attributed less weight to the unreliable and unknown fault-slip data decided by the relevance of fault-slip data. Several open-source paleostress analysis programs allow giving individual fault-slip datum weights based on the quality of fault-slip data.

Slickenside kinematic indicators

The faults are exposed in uniform lithology in the study area, therefore offset markers do not exist. The slip-sense of faults can be determined in such terrains using slickenside kinematic indictors developed over the fault planes (e.g., Hancock 1985; Petit 1987; Doblas 1998; Vanik et al. 2018; Shaikh et al. 2020; Maurya et al. 2021). Over the slip surfaces, local crystallisation/growth of calcite slickenfibers can be observed. They resemble congruous accretion steps, with risers that are essentially perpendicular to the slip direction and step-like geometry that faces in the movement direction of the missing block. Thus, in most cases, the slip planes follow the positive smoothness criterion of Angelier (1994). Calcite crystallization over the slip planes appears to have occurred concurrently with the formation of the accretion steps, implying (high-temperature) fluid flow during faulting. In the present study, depending on their morphology, calcite slickenfibers are divided into the structures as per Petit (1987), which are detailed in the following sub-sections.

Fig. 5 **a** Modified diagram of PT structures after Petit (1987), denoting criteria for determining sense of movement of the missing block. **b** Fault with normal dip-slip and sinistral strike-slip components (attitude: N40°E/55°SE and lineation attitude: 19°/N44°E). **c** Normal fault (attitude: N130°E/70°SW and lineation attitude: 61°/S90°W). **d** Fault with sinistral strike-slip and normal dip-slip components (attitude: N105°E/80°NE and lineation attitude: 15°/N72°W). **e** Fault with reverse dip-slip and sinistral strike-slip components (attitude: N160°E/60°SW and lineation attitude: 27°/N37°W). **f** Normal fault (attitude: N120°E/42°SW and lineation attitude: 39°/S55°W). **g** Dextral fault (attitude: N190°E/66°NW and lineation attitude: 16°/S28°W). **h** Sinistral fault (attitude: N80°E/34°NW and lineation attitude: 02°/N67°E). Black arrows: motion of the missing block
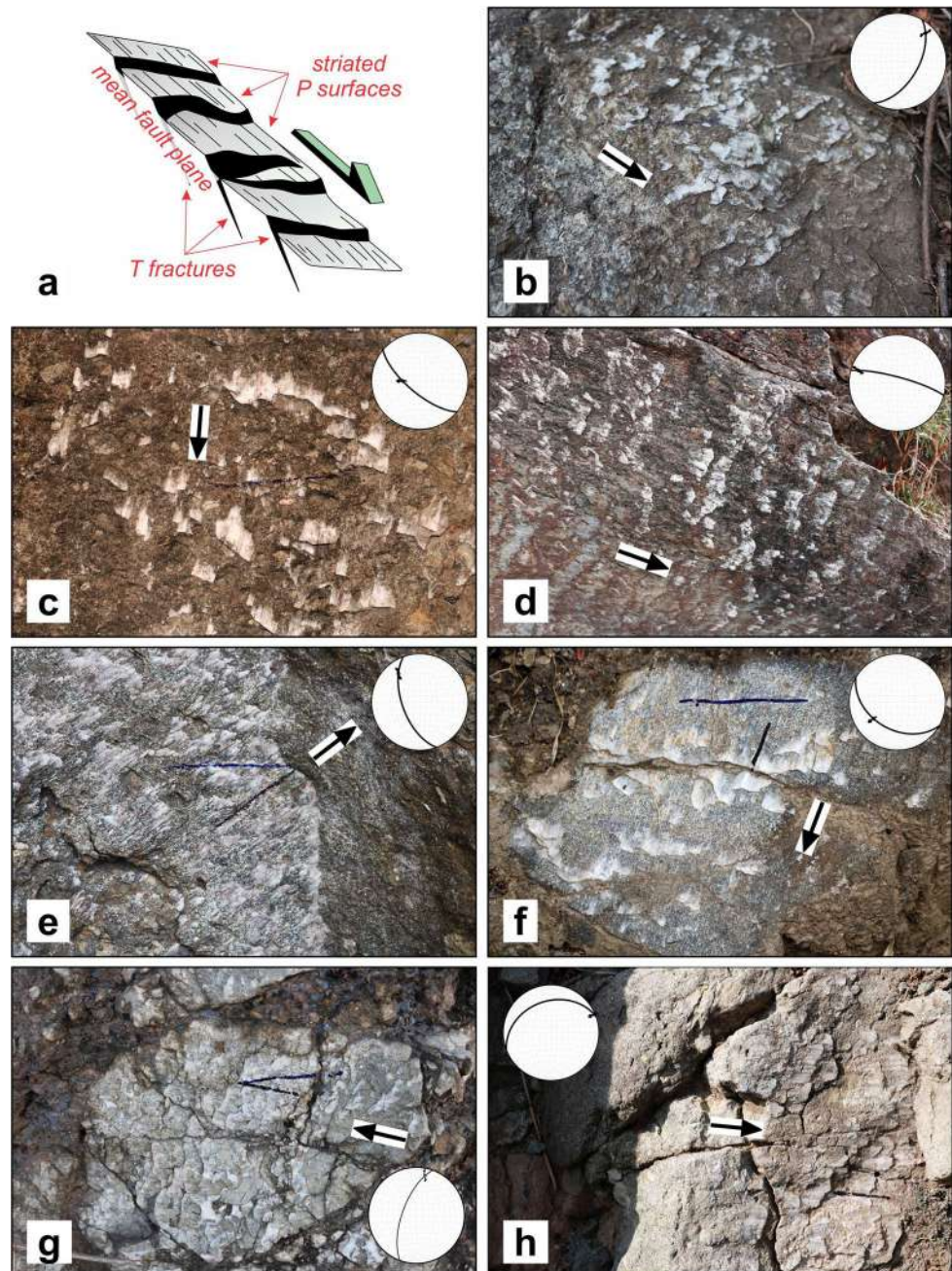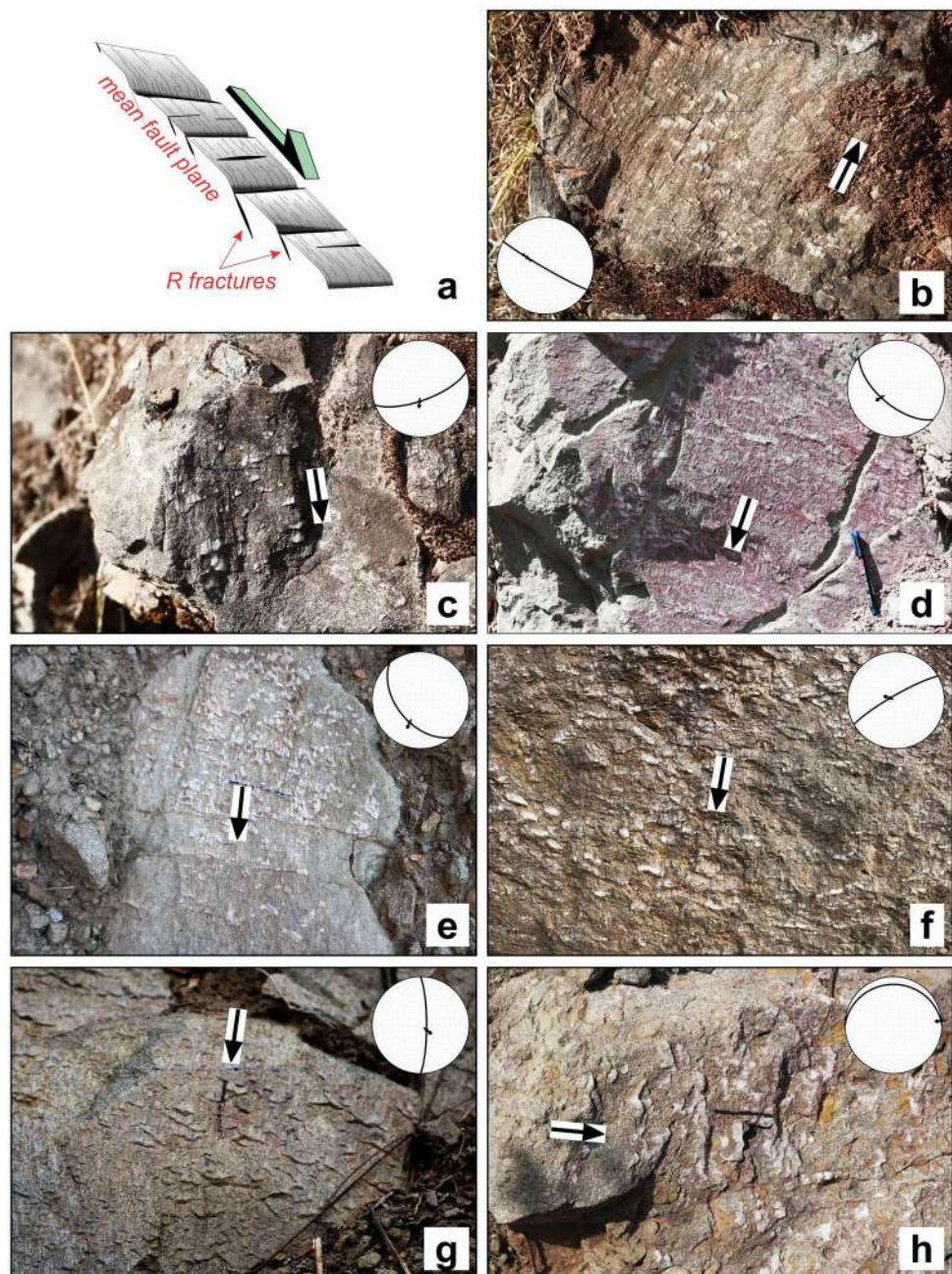
PT structures of Petit ([1987](#))

These structures (Fig. 5a) can indicate micro-seismicity (Petit [1987](#)). The slip planes are either partially striated (/non-striated) (Fig. 5b–d, f) or fully striated (Fig. 5e, g, h). The apex of the dihedron, formed by the intersection between the P and the T-surfaces shattered to form several small steps (Petit [1987](#)). The striated P-surfaces with calcite steps ascending in the direction of the missing block can be used to detect the fault slip-sense. Well-developed T-fractures sometimes are wavy (e.g., Fig. 5g, h). T-fractures have a low-angle to the mean fault plane and they dip towards the lee-side of fault asperities. The striated P-surfaces are represented by the calcite slickenfibers. Their step-like geometries indicate the motion of the missing block. For example, in Fig. 5c, the striated P-surfaces descending downward indicate normal dip-slip motion, and upward descend in Fig. 5e indicate reverse dip-slip and sinistral strike-slip components.

RM structures of Petit ([1987](#))

The RM structures (Fig. 6) are found over fully striated or non-striated slip planes. The mm- to cm-scale R shears occur at the lee side of small fault asperities that form

Fig. 6 a Modified diagram of RM structures after Petit ([1987](#)), denoting criteria for determining the sense of movement of the missing block. **b** Fault with reverse dip-slip and sinistral strike-slip components (attitude: N120°E/86°SW and lineation attitude: 124° rake). **c** Normal fault (attitude: N070°E/45°SE and lineation attitude: 45°/N174°E). **d** Fault with normal dip-slip and dextral strike-slip components (attitude: N130°E/62° and lineation attitude: 61°/S59°W). **e** Normal fault (attitude: N150°E/50°SW and lineation attitude: 47°/S26°W). **f** Normal fault (attitude: N50°E/82°NW and lineation attitude: 79°/N71°W). **g** Normal fault (attitude: N15°E/80°E and lineation attitude: 77°/N129°E). **h** Sinistral fault (attitude: N90°E/17°N and lineation attitude: 01°/N85°E). Black arrows: motion of the missing block
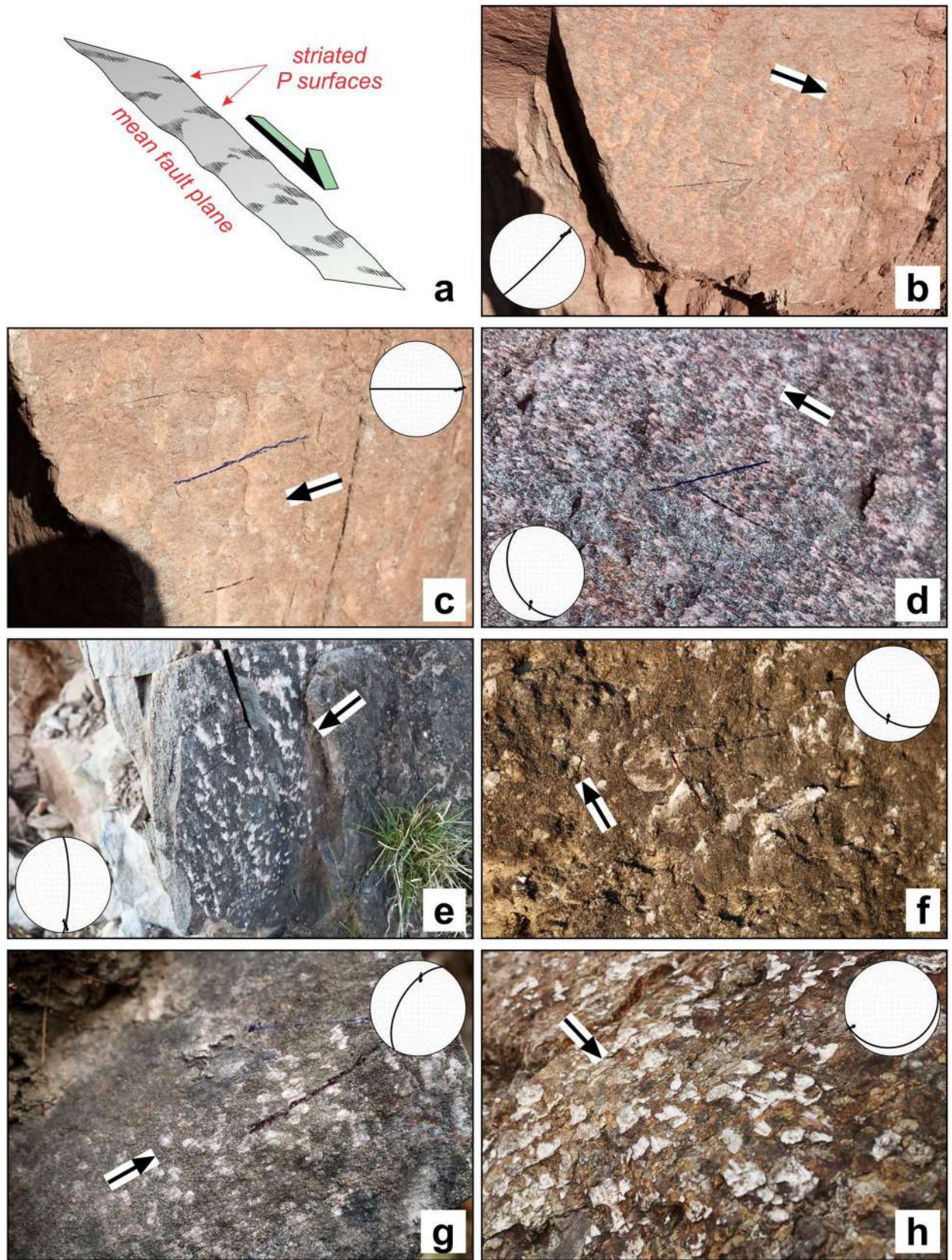
congruous steps in the direction of motion of the missing block. The R shears are dispersed unevenly over the slip planes, few being far away (Fig. 6c, d) and other quite close (Fig. 6e, f). In some cases, R shears are observed dipping at high-angle into the main fault plane and at the tip of the calcite steps (Fig. 6g, h). The RM structures differ from PT structures in the sense that the R shears are not low-dipping and also, the striated surface at the stoss-side of the steps does not ride over the next step. The distance between the R shears is more than the distance between T surfaces in PT structure found in other fault planes.

PO structures of Petit (1987)

PO structures exhibit a feeble growth of calcite slickenfibers compared to the other slip planes (Fig. 7a–d). However, due to friction during faulting, the P-surfaces on the fault plane have worn away and are now parallel to the mean fault plane. The slip planes are essentially non-striated (Fig. 7e, f). Peaks of feebly occurring striated P-surfaces point towards the direction of the missing block. The calcite steps with striated P-surfaces are very few in the case of PO structures (Fig. 7g, h). As the broken surface at the tip of steps does not dip towards the fault plane, the convex shape at the tip of the steps denotes the direction of movement of the missing block.

Field-derived data

We determined the main fault sets based on the obtained field data that can be categorized into ~ NW-striking normal slip planes and ~ NE-striking reverse slip planes. Both the major fault sets accommodate a component of strike-slip motion. The study area was divided into four sectors and grouped the structural stations based on their location in relation to the tectonic elements previously known and inferred from the geomorphic studies: sector 1 near the central segment of the BkT encompassing four structural sites, sector 2 near the out-of-sequence thrust covering six structural sites, sector 3 near the western extremity of the

BkT encompassing four structural sites, and sector 4 near the Sabilpur Active Fault (SAF) covering three structural sites.

Sector 1 (sites 14–17)

Site 14 in sector 1 shows several NW/N-striking low-angle normal slip planes. Slip planes with reverse slip do not occur at site 14. W–WNW-striking strike-slip faults occur at site 15. Few normal slip planes with NE-strike occur at site 15. Both dextral and sinistral strike-slip faults occur here with moderate to high dip. Two dominant fault-slip sets occur at site 16, NW–NNW-striking normal and reverse slip planes. Site 17 dominantly shows low-angle ~ W-striking sinistral strike-slip faults.

Sector 2 (sites 8–13)

Normal slip planes dominate here. Site 8 shows NW-striking normal slip planes with both low and moderate dip. In addition, along NW-strike, low-dipping reverse slip planes are recorded. NW-striking low-dipping slip planes with unknown kinematics potentially belonging to the dominant fault set occur in site 8. Only one NW-striking slip plane shows normal slip at site 9. Almost W-striking slip planes with reverse-slip dominate at site 9. Sites 10–13 are characterized by two dominant fault-slip sets of normal slip planes: (i) NW-striking low–moderately dipping slip planes with normal slip-sense, with a few showing minor strike-slip component; and (ii) NNE–NE-striking high-angle slip planes with normal slip-sense.

Sector 3 (sites 4–7)

Sector 3 is characterized by the dominant occurrence of normal slip planes, mainly at structural sites 4, 5 and 6, exposed in Lower Siwalik sandstones. Two dominant sets at structural site 4 are recorded comprising (i) WNW–NW-striking high-angle normal slip planes, and (ii) NE-striking reverse slip planes. Alternatively, few NNE–NE-striking slip planes with dextral/sinistral strike-slip are observed. At site 4, the intersection of the bedding plane with the slip plane produces a slickenline-like appearance. Care was taken to ensure that such structures were not documented in the field data. The high-angle structures recorded at structural site 5 are divided into three fault-slip sets: (i) NW–WNW-striking normal slip planes, (ii) NW-striking reverse slip planes, and (iii) NNE–NE-striking normal slip planes. NW-striking oblique-slip planes with the major normal dip-slip component are the most notable structures in sector 3. The structural site 6 dominantly expose low–moderate-angle NE–ENE-striking normal slip planes with a minor dextral strike-slip component. Few NW-striking high-angle reverse

slip planes with a minor sinistral strike-slip component are also observed. Site 7 is dominated by NW-striking reverse slip planes and near-vertical N-striking dextral slip planes.

Sector 4 (sites 1–3)

This sector shows dominantly moderate to high-angle NE–NNE-striking reverse slip planes. The other prevalent set consists of NW/NNE/NE-striking slip planes with unknown kinematics (line-only fault-slip data). This dominant set is more prominent in structural sites 2 and 3 are characterized by, whereas structural site 1 mostly exposes reverse slip planes. Other than the slip planes with unknown slip-sense, structural sites 2 and 3 encompass NW-striking and NE-dipping sinistral strike-slip faults.

Paleostress analysis using T-Tecto Studio X5 software

Fault-slip analysis was performed by implementing the multiple slip inverse method in T-Tecto Studio X5 (Žalohar and Vrabec 2008) and 25 reduced paleostress tensors were obtained. Inversions with less than five fault-slip data from a structural data are poorly constrained and are not included in the analysis. To achieve the best-fit reduced paleostress tensor, the angular misfit between the anticipated slip direction and striation direction was kept $\leq 20°$ (Federico et al. 2014; Tranos 2017; Shaikh et al. 2020). Each of the six modifiable parameters in T-Tecto Studio X5 was adjusted independently to see how they affected the stability of the resultant paleostress tensor (Žalohar and Vrabec 2008).

To monitor for spatial changes in paleostress orientation, data from different transects are not merged for paleostress analysis. Separation of polyphase heterogeneous fault-slip data into homogeneous subsets was performed in T-Tecto Studio X5. If fault-slip data are taken from faults triggered by spatially or temporally different stress conditions, such fault-slip data are called heterogeneous (Yamaji and Sato 2019). To understand the heterogeneous dataset, multiple stress states are required (Yamaji and Sato 2019). Fault slip-data are considered homogeneous if all the data are described by a single stress condition (Yamaji and Sato 2019). To map the faulting styles and relative stress regime across the study region, we utilize the R' stress ratio as per Delvaux et al. (1997) that ranges from 0 (uniform horizontal extension with $S_V > S_{Hmax} = S_{Hmin}$) to 1.5 (strike–slip faulting with $S_{Hmax} > S_V > S_{Hmin}$) to 3 (uniform horizontal compression with $S_{Hmax} = S_{Hmin} > S_V$). S_V, S_{Hmax}, S_{Hmin} are the standard symbols used in rock mechanics and structural geology to indicate the principal stress axes that are vertical, and horizontal in two perpendicular directions, respectively. Out of the two horizontal components, the one with a higher magnitude is stated as S_{Hmax} and that with the lower magnitude as S_{Hmin}. The tectonic stress regime index R' is defined as:

$R' = R$ (for normal faulting regime).
$R' = 2 - R$ (for strike-slip faulting regime).
$R' = 2 + R$ (for reverse faulting regime).

Results

Geomorphology

Linear surface expression and topographic profiles

The identified fault line is traceable as an outstanding linear feature observed over > 10 km on a Digital Elevation Model (Figs. 2, 8). The linear trace spatially corresponds to a sudden break in slope elaborated by a sudden change in contour spacing on either side of the surface trace (Fig. 8). Such a break in slope of the cumulative scarp (~ 400 m over 1.25 km to ~ 25 m over 1 km) across the linear trace is suggestive of active faulting and uplift along the fault (Silva et al. 2003; Singh and Virdi 2007).

The topographic swath profiles (showing mean, max. and min.) drawn across the sub-Himalayan belt in the central part of the Nahan salient shows the range of surface elevations from ~ 300 m towards the foreland in the south to ~ 1000 m towards the hinterland in the north (Figs. 2, 3). In the plains to the south of the MFT, the three profiles are closely-spaced (Fig. 3). However, this is not the case in the north of MFT where the three sets of profiles are distinct and are characterized by variable distribution range in between the minimum and the maximum elevations. Abrupt change in the elevation profile and the offset between the three profiles characterize the active tectonic control on the topography. The abrupt change is observed across sites marked as MFT, NT/BkT, Tikkar Tal Thrust (TTT) and BiT (Fig. 3). In all these cases the swath profile tends to widen across the thrust fault in its hangingwall. Contrarily, it remains narrow in the footwall. This is most distinctly seen for the MFT because it also marks a boundary of transition between the basic geomorphic units of hills and plains. Of course, not so distinct there are similar signatures present at the BkT, TTT and BiT. This suggests an ongoing topographic adjustment in response to the active tectonic deformation along these thrust faults, respectively. All these observations are spatially consistent with the increased local relief (Fig. 3).

Two topographic swath profiles (showing mean, max. and min.) were drawn along the fault line TTT, in its hangingwall and footwall. The swaths range is 500 m (Fig. 4). The elevations in the hanging wall are higher than the footwall. This is also evident in the relief profiles in the two fault blocks. The actively uplifting hangingwall block displays higher relief in comparison to the footwall block,

Fig. 8 Spatial distribution maps show the new faultline, as in Fig. 2. **a** The knickpoints are present in the hanging wall of the fault. **b** Abrupt change in contour spacing across the fault-line. **c** Ksn values along streams increase abruptly very close to the faultline
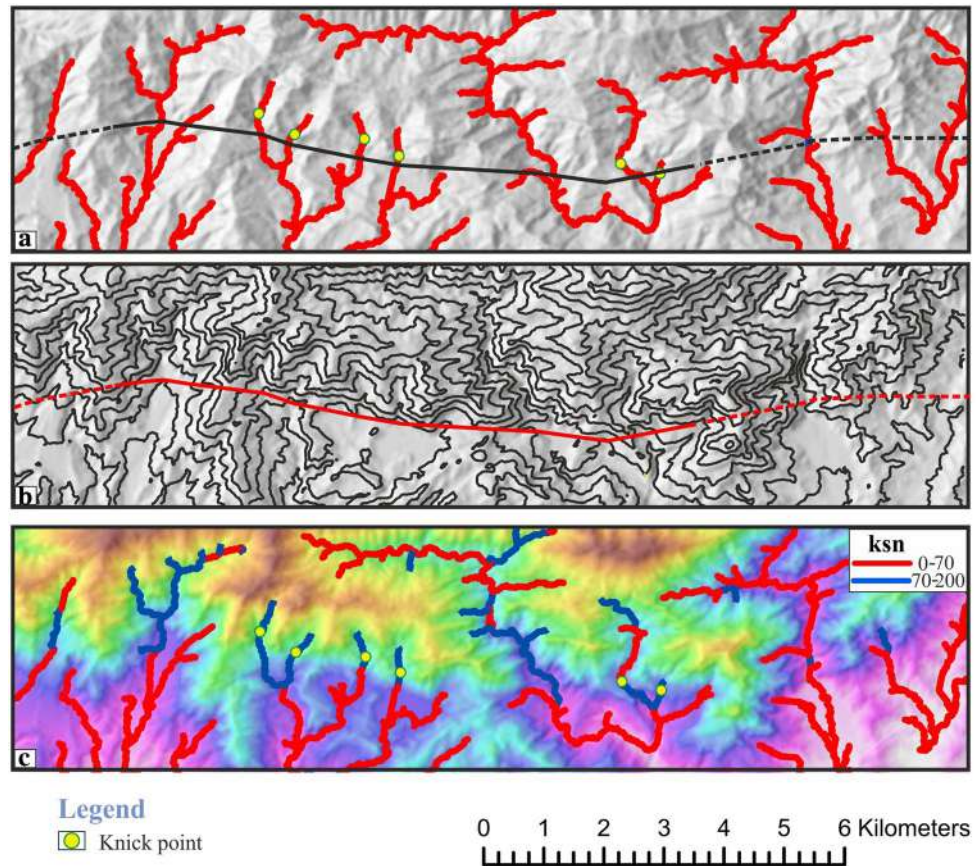
thereby suggesting active incision in the footwall block in response to the active uplift.

### Normalized steepness (K_sn) index

This index has been widely used as a reliable proxy to tectonically-induced perturbations in river longitudinal profiles (Kirby and Whipple 2012; Jaiswara et al. 2020). It is an advanced derivative of the simple longitudinal profile, which is calculated for all the streams crossing the faultline TTT. For the identified segments, the K_{sn} values vary from 0 to > 200. They are classified into two classes i.e. 0–70 (low) and 70–200 (high). These classes are distributed on either side of the identified faultline separated by a knickpoint (Fig. 8, Fig. S2). The calculated knickpoints for each of these streams mostly lie either close to the faultline or slightly upstream suggesting an upstream migration of the knickpoints (Fig. 8, Fig. S2). In this case, without any lithological contrast across the knickpoint it can be manifested as channel narrowing in areas of high uplift rate (Whittaker and Boulton 2012; Kumar 2012).

Fault-slip analysis results

The study area is characterized by the presence of variably striking low- to high-angle dip-slip, strike-slip and oblique-slip faults. Site-wise field observations are detailed in the supplementary material (Figs. S3–S11). To calculate the paleostress tensor, at least four fault-slip data are required, and therefore, we incorporated such 17 structural sites in the fault-slip inversion procedure that meet this requirement. Figure 9 presents the T-Tecto results. The fault-slip populations at most of the structural sites are heterogeneous, i.e., they do not fit into a single paleostress tensor, and they reflect temporal changes in the paleostress field. T-Tecto program successfully separated heterogeneous fault-slip data into homogeneous sub-sets, as evidenced by the results. Fault-slip data that misfit with the resultant paleostress tensors were discarded and are not included in the results.

At some sites, two phases of deformation involving normal and reverse dip-slip motion and associated strike-slip components have been observed. The fault-slip inversion technique described previously suggests three brittle deformations operating over the Panchkula-Morni region, which is discussed below.

Fig. 9 The reduced stress tensors were generated for a total of 17 fault-slip data sites using Multiple Slip method implemented in T-Tecto studio X5 (Zalohar and Vrabec 2008). Black lines: fault planes with slip vectors marked by a black dot with arrows. Red and blue quadrants: compressive and extensive stress fields, respectively. Biggest, medium and smallest square symbols: orientation of maximum (σ_1), intermediate (σ_2) and minimum (σ_3) stress axes respectively ($\sigma_1 \geq \sigma_2 \geq \sigma_3$). Largest, intermediate and smallest yellow circles: directions of principal strain axes measured by Visualization of Gauss Function method. Red (and black) inward and blue (and black) outward arrows: direction of compressive and tensile stress, respectively. Black arrows pointing inward and pointing outward at the periphery of the stereoplots: orientation of maximum (S_{Hmax}) and minimum (S_{Hmin}) horizontal principal stress respectively. Site numbers are shown on the upper left of paleostress tensors. Stereoplots with discarded fault-slip data having misfit angle $> 20°$ are also shown
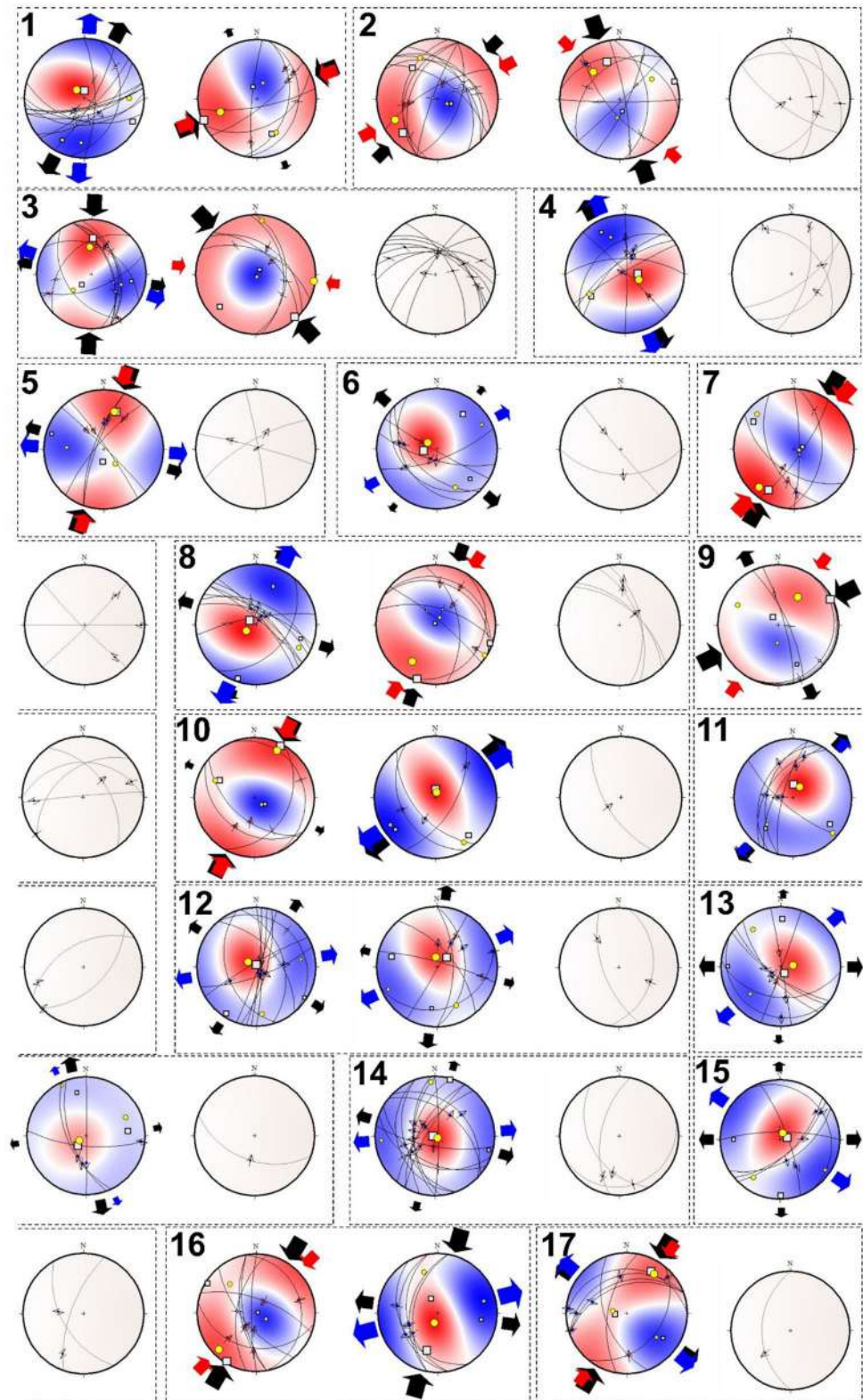
The individual deformation events are distinguished based on the homogeneity among the deduced paleostress tensors in terms of the attitude of principal stress axes and stress ratio. These are: (i) NW extension, (ii) NE to ENE extension, and (iii) NE compression.

Extensional stress field with NW extension

Low-angle W–WSW-striking sinistral slip planes and NNE-striking normal slip planes in sector 1 are formed under the extensional stress field with stress regime index $R' = 0.3$. The paleostress tensor shows oblique normal kinematics (oblique σ_1-axis, NE–SW trending σ_2, and NW–SE trending σ_3). No structural sites in sector 2 have generated normal or oblique normal slip planes with NW extension. Only site 4 in sector 3 shows NE-striking normal faults formed under the NW-oriented extension. The corresponding paleostress tensor gives $R' = 0.4$ with oblique σ_1, and sub-horizontal σ_2 and σ_3 axes.

Extensional stress field with NE–ENE extension and NW–NNW compression

In sector 1, no normal slip planes were generated under NE-oriented extension. NW-striking normal slip planes at sites 8 and 10 in sector 2 are formed under NE extension with $R' = 0.1$. The low rake of a few normal slip planes accommodates a minor component of sinistral strike-slip. The paleostress tensor shows oblique σ_1-axis (azimuth/plunge: 300–003°/65–76°), a sub-horizontal σ_2 (azimuth/plunge = 139–198°/03–14°), and a sub-horizontal σ_3 (108–231°/10–20°). The vertical plunge of σ_1-axis at site 10 indicates the role of a pure extensional stress field with NE-oriented extension.

Compressional stress field with NE compression and NW extension

Sites 16 and 17 in sector 1 show dominantly NW–NNW-striking reverse slip planes generated under NE-directed compression with $R' = 2.5$ to 2.7. The paleostress tensor shows horizontal σ_1-axis (azimuth/plunge: 211°/02°), horizontal σ_2 (azimuth/plunge: 301°/02°), and a nearly vertical σ_3 (azimuth/plunge: 77°/87°). Sites 8 and 10 in sector 2 show the paleostress tensors with NE-directed compression and $R' \sim 2.5$ indicating the role of the pure compressional stress field. The paleostress tensor shows horizontal σ_1-axis (azimuth/plunge: 027°/02°), σ_2 with an azimuth/plunge of 296°/24°, and an oblique σ_3 (azimuth/plunge: 122°/66°). Sites 5 and 7 in sector 3 show paleostress tensors with NE-directed compression. The oblique plunge of σ_3-axis indicates the role of transpressional to compressional stress field to generate the NW-striking reverse-slip planes with a minor dextral strike-slip component. In sector 1, sites 1 and 2 show NE–ENE compression with $R' = 2.2$–2.5, which generated NW–NNE-striking reverse slip planes.

Additional constraints from seismic images in Powers (1997)

The reflection seismic data originally procured by the ONGC has been used by several workers for processing and re-processing, which has led to improved interpretations and re-interpretations of geological structures and structural geometries (Powers 1997; Powers et al. 1998; Mukhopadhyay and Mishra 1999; Raiverman et al. 2002; Dutta et al. 2019). We followed the Geological Survey of India's map, performed field checks, and based on the reconciliation of geology and a seismic profile; the Tikkar Tal Thrust (TTT), as we name it, is located in between the BkT and BiT (Figs. 2, 10).

Discussions

Geomorphologic issue

The observed surface topography in the central part of the Nahan salient is mainly controlled by the surface trace of the BkT, which carries the Lower Siwalik in the thrust sheet. The thrust forms a curved trace, which is wider in the central part and narrows on the extremes (Figs. 1, 2). Geometrically, this means that the BkT strikes NW–SE in the central part whereas it changes its strike on either side to cut-up section and join the BiT. In the western part, the strike is NNW–SSE whereas it is NNE–SSW in the eastern part. Assuming the general Himalayan tectonic transport direction to be towards S/SW, the BkT geometry should generate an oblique movement on both its extremes away from the central part, where the movement should be ideally normal.

This type of structural geometry would allow the BkT sheet to travel further in the central part and therefore it is wider there. However, oblique movement on either extremes would limit its transport as a function of dip of the thrust. Therefore, the thrust sheet narrows at the extremes (Fig. 2). In turn, the distance between the BkT and BiT would be higher in the central part than on either side. As the BkT sheet has more slip in the central part, this geometry poses a mechanical constraint, which would need to be accomplished either by folding or faulting the rock as elaborated further. First, it would be difficult to transport high dips over long distances without appropriate structural support and so it would require a reduction in dip towards the leading edge of the thrust sheet. Similar reduction in dips has been observed from the surface topography, in field and also on seismic profiles (Figs. 2, 10). Therefore, the structural geometry of the thrust sheet with varying dip domains that gradually become gentler towards the front of the thrust sheet is a consequence of a multi-bend fault bends folding (Mukhopadhyay and Mishra 1999).
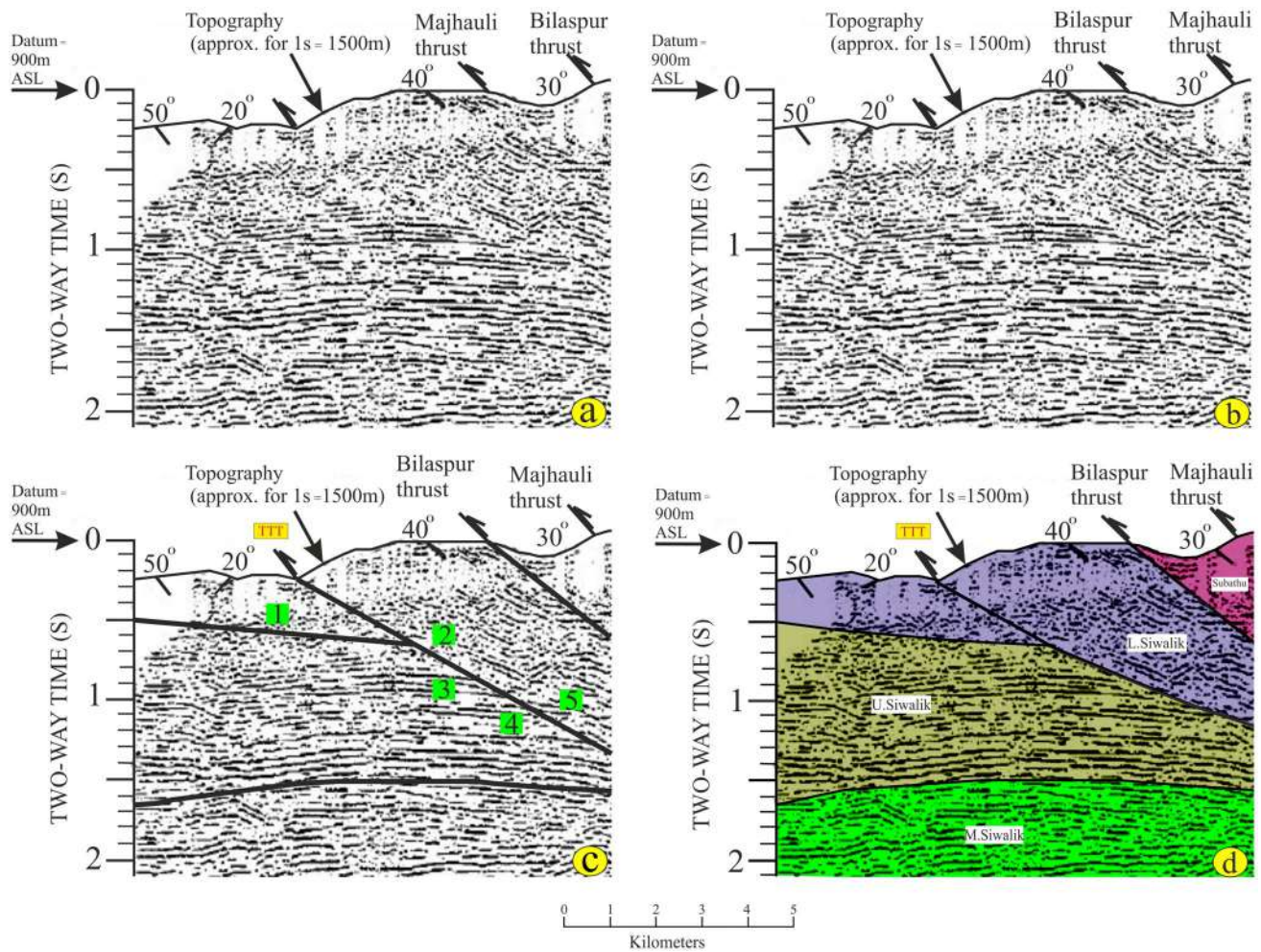
Fig. 10 Additional constraints from seismic reflection data along the yellow line in Fig. 2. and interpretations from Powers (1997). **a** Part of the profiles as published in Powers (1997). **b** A reconciliation of the geological map in Fig. 2 and the reflection profile suggests that the names of thrust faults (BiT and MjT) were interchanged inadvertently. The correct version is shown here. **c** The interpretation of fault-lines is adopted from Powers (1997), now shown with the corrected thrust names. Numbers 1 to 5 show different reflection patterns across the faultlines. **d** Seismic profile colour coded for lithology (labels shown in the figure) to project the juxtaposition of geology and structure. The newly identified TTT is shown. For seismic image interpretation see Misra and Mukherjee (2018)

However, this renders a degree of geometrical complexity to the thrust sheet deforming at shallow levels. Any further compression within or below the thrust sheet would actually make the geometry more complex, which is not tenable in such brittle/shallow deformation environments and would have to respond by a breakthrough thrust along the steeper limb of the Fault-Bend Fold as seen in the BkT thrust sheet. A similar geometry can be seen on the seismic profile where it appears to breach the anticline in the BkT sheet by an out-of-sequence thrust fault (Fig. 10; modified from Powers 1997). The out-of-sequence thrust fault hypothesis is consistent with the topographic and structural observations (see Mukherjee 2015). This hypothesis is also supported by the fact that the out-of-sequence thrust (OOST) merges with the BkT on the surface on either side as the thrust sheet narrows laterally (Fig. 2). In addition, the present-day surface

topography testifies that the OOST within the BkT thrust sheet is an active fault.

Structural issues

Almost all the structural sites are characterized by the heterogeneous fault-slip population. Sector 1 is located in the upthrown block and near the BkT, where the striated slip planes are exposed within the Upper Siwalik sandstones. The paleostress analysis results at site 15 indicate that the slip planes are generated under the extensional stress field with $R' = 0.5$ and NW-oriented extension (Fig. 9). A sub-vertical σ_1 (azimuth/plunge: 077°/76°), a sub-horizontal σ_2 (azimuth/plunge: 179°/03°) and a sub-horizontal σ_3 (azimuth/plunge: 270°/14°) define the extensional stress field. An extensional stress field is indicated. The local-scale

stress regime generated (i) NNE- to NE-striking faults with normal slip, and (ii) NW- to NNW-striking faults with sinistral and dextral slip. No reverse slip-sense was found on any of the slip planes, which could support the geometry of the NW-striking BkT in its central segment. Fault-slip measurements and analysis at sites 16 and 17 suggest that the extensional stress field at site 15 is replaced by a pure compressive stress field with $R' = 2.5$ and the dominant NE-oriented compression (Fig. 9). The compressional stress field has generated (i) NW–NNW-striking and low–moderately dipping slip planes with reverse slip.

Occasionally, along with the major reverse dip-slip component, several slip planes experienced sinistral/dextral strike-slip. (ii) NNE–NE-striking slip planes could not experience reverse slip under the NE-directed compression and therefore resolved into the normal slip-sense. The compressional stress field is characterized by a sub-horizontal σ_1 with an azimuth/plunge of 211°/02°, a sub-horizontal σ_2 with an azimuth/plunge of 301°/02°, and near-vertical σ_3 with an azimuth/plunge of 077°/87°. The dominant stress field in this region is NE-directed compression. It is possible that it had a significant influence on the generation of NW-striking BkT in its central segment. Thus, in addition to the direct structural evidence, the estimated tectonic stress regime has also been inferred from the geomorphic analysis, suggesting that NE compression has most likely continued to the present day.

The structural sites are located in sector 3 at the western extremity of the BkT, where the slip planes are exposed in the Lower Siwalik. In this segment, (i) NW-striking oblique-slip planes with major normal slip and minor dextral strike-slip components, (ii) NE–E-striking slip planes with normal slip, and (iii) NNW–NW-striking oblique-slip planes with major reverse slip and minor dextral/sinistral strike-slip components are documented. In contrast to the central segment of the BkT, where NE–E-striking normal slip planes are abundant, the western extremity of the BkT has a greater number of NW-striking oblique-slip planes with major normal slip. The NE–E-striking normal slip planes are less numerous at the western extremity of the BkT. Under the extensional stress field with $R' = 0.2$, NW-striking oblique-slip planes with major normal slip and minor dextral strike-slip components are generated (Fig. 9).

The NW-directed extension direction in the central segment of the BkT swings to NE near its western extremity. The extensional stress field is characterized by a sub-vertical plunge of σ_1 changing to oblique with 261°/65°, a sub-horizontal σ_2 with an azimuth/plunge of 037°/19°, and a nearly horizontal σ_3 with an azimuth/plunge of 133°/16° (Fig. 9). The oblique plunge of the σ_1-axis and dominant

NE extension direction may therefore be responsible for the oblique movement with major normal slip at the western extremity of the BkT, which confirms our geomorphic interpretations. Other than the normal slip, another major component observed at the western segment of the BkT are the NNW–NW-striking striated slip planes with major reverse slip and minor dextral/sinistral strike-slip components formed under the transpressional stress field with NE oriented compression and $R' = 2.1$.

In sector 2, the structural sites located in the vicinity of the OOST expose: (i) W–NW-striking reverse slip planes with minor dextral strike-slip component, (ii) WNW–NW-striking normal slip planes with minor sinistral strike-slip component, and (iii) NNE–NE-striking normal slip planes. W–NW-striking reverse slip planes are developed under NE-directed compression under compressional stress field with R' ranging from 2.2 to 2.7. At site 8, the compressional stress field is characterized by a sub-horizontal σ_1 with azimuth/plunge: 027°/02°, σ_2 with 296°/24°, and an oblique σ_3 with 122°/66° (Fig. 9). The fault-slip analysis results at site 10 are characterized by a sub-horizontal σ_1 with an azimuth/plunge of 199°/02°, a sub-horizontal σ_2 with an azimuth/plunge of 109°/02°, and a sub-vertical σ_3 with an azimuth/plunge of 334°/87° (Fig. 9). The oblique plunge of σ_3 at site 8 indicates the role of the dextral strike-slip component. The fault-slip analysis results at site 10 correlate well with the geometry of the NW-striking OOST, when compared to those at site 8.

WNW–NW-striking slip planes near the OOST are developed under the extensional stress field with NE-oriented extension and R' ranging from 0.1 to 0.7. The corresponding attitude of principal stress axes are: σ_1 with an azimuth/plunge of 300–003°/76°, σ_2 with an azimuth/plunge of 139–198°/03–11°, and σ_3 with an azimuth/plunge of 108–231°/10–14° (Fig. 9). NNE–NE-striking normal slip planes at sites 11 and 12 are formed under the extensional stress field with NE–ENE directed extension and $R' = 0.3$. The corresponding attitude of principal stress axes are: σ_1 with an azimuth/plunge of 003–046°/65–86°, σ_2 with an azimuth/plunge of 126–213°/03–15°, and σ_3 with an azimuth/plunge of 122–221°/02–20° (Fig. 9).

Relict structures have been documented from poly-deformed terrains (e.g., Mukherjee and Koyi 2010; Mukherjee 2013; Dutta and Mukherjee 2019). Why and how the prior deformation-induced structures, fault planes and lineations, remained preserved in the present study area remain a subject of future research.

Conclusions

Slickenside kinematic indicators viz., PT, RM and PO structures helped in interpreting the movement of the slip planes exposed in the uniform lithology. Paleostress analysis

results show the dominance of two end-member of tectonic stress regimes: extensional stress field with NE–ENE and NW oriented extension, and NE-oriented compression. The compressional stress field with NE compression is consistent with the geometry of BkT inferred from the geomorphic analysis. The NE extension direction and oblique plunge of the σ_1-axis may be responsible for the oblique movement with major normal slip at the western extremity of the BkT.

Abrupt change in topographic swath profiles and their mutual offset indicate active tectonics. Such changes are observed across sites for already known faults e.g., MFT, NT/BkT and BiT, and also for the newly reported active fault Tikkar Taal Thrust (TTT). The geomorphologic and morphometric analyses led us to confirm that TTT is an out-of-sequence active fault that occurs within uniform lithology of sandstone in the central part of the Nahan salient. We could also locate TTT in the previously published seismic section. Presence of TTT mainly in sectors 2 and 3 is corroborated by the presence of NE compressional structures.

References

Angelier J (1994) Fault slip analysis and palaeostress reconstruction. In: Continental deformation. Pergamon Press, pp 53–100

Bose N, Mukherjee S (2020) Estimation of deformation temperatures, flow stresses and strain rates from an intra-continental shear zone: the Main Boundary Thrust, NW Himalaya (Uttarakhand, India). Marine Petrol Geol 112:104094

Caputo R (2005) Ground effects of large morphogenic earthquakes. J Geodyn 40:113–118

Cooper M (2007) Structural style and hydrocarbon prospectivity in fold and thrust belts: a global review. In: Ries AC, Butler RWH, Graham RH (eds) Deformation of the continental crust: the legacy of mike coward, vol 272. Geol Soc, London, Spec Publ, pp 447472

Craig J, Hakhoo N, Hafiz M, Khan MR, Misra R, Pandita SK, Raina BK, Thurow J, Thusu B, Ahmed W, Khullar S (2018) Petroleum systems and hydrocarbon potential of the North-West Himalaya of India and Pakistan. Earth Sci Rev 187:109–185

Delvaux D, Moeys R, Stapel G, Petit C, Levi K, Miroshnichenko A, Ruzhich V, San'kov V (1997) Paleostress reconstructions and geodynamics of the Baikal region, central Asia, Part 2. Cenozoic rifting. Tectonophysics 282:1–38

Dey S, Thiede RC, Schildgen TF, Wittmann H, Bookhagen B, Scherler D, Strecker MR (2016) Holocene internal shortening within the northwest Sub-Himalaya: out-of-sequence faulting of the Jwalamukhi Thrust, India. Tectonics 35:2677–2697

Doblas M (1998) Slickenside kinematic indicators. Tectonophysics 295:187–197. https://doi.org/10.1016/S0040-1951(98)00120-6

Doblas M, Mahecha V, Hoyos M, Loīpez-ruiz J (1997) Slickenside and fault surface kinematic indicators on active normal faults of the Alpine Betic cordilleras, Granada, southern Spain. J Struct Geol 19:159–170. https://doi.org/10.1016/S0191-8141(96)00086-7

Dutta D, Samanta BG (2008) 2D thermal modeling over a structurally balanced cross section within the Median Belt of Outer Himalaya, Himachal Pradesh, India. Assoc Petrol Geol Bull 2:195–204

Dutta D, Mukherjee S (2019) Opposite shear senses: geneses, global occurrences, numerical simulations and a case study from the Indian Western Himalaya. J Struct Geol 126:357–392

Dutta D, Biswas T, Mukherjee S (2019) Arc-parallel compression in the NW Himalaya: Evidence from structural and palaeostress studies of brittle deformation from the clasts of the Upper Siwalik, Uttarakhand, India. J Earth Syst Sci 128:125

Federico L, Crispini L, Vigo A, Capponi G (2014) Unravelling polyphase brittle tectonics through multi-software fault-slip analysis: the case of the Voltri Unit, Western Alps (Italy). J Struct Geol 68:175–193

Gill HS, Singh T, Singh S, Kim JR, Caputo R, Kaur G, Khosla A (2021) Active transfer faulting in the NW Sub-Himalaya (India) observed by space-borne topographic analyses. Quat Int 85:15–26

Goffey G, Craig J, Needham T, Scott R (2010) Fold–thrust belts: overlooked provinces or justifiably avoided? In: Goffey GP, Craig J, Needham T, Scott R (eds) Hydrocarbons in contractional belts, vol 348. Geol Soc, London, Spec Publ, pp 1–6

Goswami T, Gogoi M, Mahanta BN, Mukherjee S, Saikia H, Shaikh M, Kalita P, Baral U, Sarmah R (2022) Brittle tectonics in the western Arunachal frontal fold belt, India: change in stress regime from pre-collisional extension to collisional compression. Geol J. https://doi.org/10.1002/gj.4393

Hammerstein JA, Di Cuia R, Cottam MA, Zamora G, Butler RWH (2020) Fold and thrust belts: structural style, evolution and exploration—an introduction. In: Hammerstein JA, Di Cuia R, Cottam MA, Zamora G, Butler RWH (eds) Fold and thrust belts: structural style, evolution and exploration, vol 490. Geol Soc, London, Spec Publ, pp 1–8

Hancock PL (1985) Brittle microtectonics: principles and practice. J Struct Geol 7:437–457

Jaiswara NK, Kotluri SK, Pandey P, Pandey AK (2020) MATLAB functions for extracting hypsometry, stream-length gradient index, steepness index, chi gradient of channel and swath profiles from digital elevation model (DEM) and other spatial data for landscape characterisation. Appl Comp Geosci 7:100033

Karunakaran C, Ranga Rao A (1979) Status of exploration for hydrocarbons in the Himalayan region-contributions to stratigraphy and structure. Oil and Natural Gas Commission, pp 1–66

Kaushal RK, Singh V, Mukul M, Jain V (2017) Identification of deformation variability and active structures using geomorphic markers in the Nahan salient, NW Himalaya, India. Quat Int 462:194–210

Kirby E, Whipple KX (2012) Expression of active tectonics in erosional landscapes. J Struct Geol 44:54–75

Kumar M (2012) What drives knickpoints to migrate upstream? Eos Trans AGU 93(25):240

Maurya DM, Shaikh MA, Mukherjee S (2021) Comment on Structural attributes and paleostress analysis of Quaternary landforms along the Vigodi Fault (VF) in Western Kachchh region [Quat Int https://doi.org/10.1016/j.quaint.2020.07.038] 601:143–147

Miccadei E, Piacentini T, Pozzo AD, La Corte M, Sciarra M (2013) Morphotectonic map of the Aventino-Lower Sangro valley (Abruzzo, Italy), scale 1:50,000. J Maps 9:390–409

Mishra P, Mulhopadhyay DK (2012) Structural evolution of the frontal fold–thrust belt, NW Himalayas from sequential restoration of balanced cross-sections and its hydrocarbon potential. In: Bhat GM, Craig J, Thurow JW, Thusu B, Cozzi A (eds) Geology and hydrocarbon potential of Neoproterozoic–Cambrian Basins in Asia, vol 366. Geol Soc, London, Spec Publ, pp 201–228

Misra AA, Mukherjee S (2018) Seismic structural analysis. In: Misra AA, Mukherjee S (eds) Atlas of structural geological interpretation from seismic images. Wiley Blackwell, pp 15–26

Mittal AK, Pandey HC, Uniyal AK, Singh RR (2006) Geochemistry of gas seeps from surface shows and wells of the Himalayan Foreland Basin. In: 6th Int Conf & Exposition Petrol Geophys, pp 235–241

Mukherjee S (2013) Deformation microstructures in rocks. Springer Geochemistry/Mineralogy. Berlin, pp 1–111

Mukherjee S (2015) A review on out-of-sequence deformation in the Himalaya. In: Mukherjee S, Carosi R, van der Beek P, Mukherjee BK, Robinson D (eds) Tectonics of the Himalaya, vol 412. Geol Soc, London. Spec Publ, pp 67–109

Mukherjee S, Koyi HA (2010) Higher Himalayan shear zone, zanskar section—microstructural studies & extrusion mechanism by a combination of simple shear & channel flow. Int J Earth Sci 99:1083–1110

Mukhopadhyay DK, Mishra P (1999) A balanced cross section across the Himalayan foreland belt, the Punjab and Himachal foothills: a reinterpretation of structural styles and evolution. Proc Ind Acad Sci Earth Planet Sci 108:189–205

Petit JP (1987) Criteria for the sense of movement on fault surfaces in brittle rocks. J Struct Geol 9:597–608

Powers PM (1997) Structure and shortening of the Kangra and Dehra Dun reentrants, sub-Himalaya, India. Dissertation, Oregon State University

Powers PM, Lillie RJ, Yeats RS (1998) Structure and shortening of the Kangra and Dehra Dun reentrants, sub-Himalaya, India. Geol Soc Am Bull 110:1010–1027

Raiverman V, Srivastava AK, Prasad DN (1994) Structural style in northwesternHimalayan foothills. Himal Geol 15:263–280

Raiverman V, Singh B, Singh MP (2002) Foreland sedimentation in Himalayan tectonic regime: a relook at the orogenic process, Dehradun, pp 1–378

Rao R (1986) North-west Himalayan foothills: its stratigraphical record and tectonic phases. Oil Nat Gas Comm Bull 23:109–128

Sato K (2006) Incorporation of incomplete fault-slip data into stress tensor inversion. Tectonophysics 421:319–330

Shaikh MA, Maurya DM, Mukherjee S, Vanik NP, Padmalal A, Chamyal LS (2020) Tectonic evolution of the intra-uplift Vigodi-Gugriana-Khirasra-Netra Fault System in the seismically active Kachchh rift basin, India: implications for the western continental margin of the Indian plate. J Struct Geol 140:104124

Sharma R (2015) An overview of geology, abnormal pressure occurrences and hydrocarbon prospectivity of Jammu foreland sub-basin, NW Himalaya. ONGC Bull 50:37–60

Silva PG, Goy JL, Zazo C, Bardajı T (2003) Fault-generated mountain fronts in southeast Spain: geomorphologic assessment of tectonic and seismic activity. Geomorphology 50:203–225

Simón JL (2019) Forty years of paleostress analysis: has it attained maturity? J Struct Geol 125:124–133

Singh T, Awasthi AK (2010) Stream profiles as indicator of active tectonic deformation along the Intra-Foreland Thrust, Nahan Salient, NW India. Curr Sci 98:95–98

Singh T, Awasthi AK (2019) Deformation in the KangraReentrant, Himachal Pradesh of NW-Sub Himalaya of India: a paradox. In: Mukhrjee S (ed) Tectonics and structural geology: indian context. Springer, Cham, pp 381–396

Singh T, Virdi NS (2007) Tectonic activity classes along the Nahan Thrust (NT) in NW Sub-Himalaya. J Ind Soc Remote Sens 35:221–230

Singh T, Sharma U, Kumar R (2007) Soft sediment deformation in the Morni Area, NW Sub-Himalaya. Curr Sci 93:1151–1155

Singh S, Parkash B, Awasthi AK (2009) Origin of red color of the Lower Siwalik palaeosols: a micromorphological approach. J Mt Sci 6:147

Singh T, Sharma U, Awasthi AK, Virdi NS, Kumar R (2011) Geomorphic and structural evidences of neotectonic activity in the Sub-Himalayan belt of Nahan Salient, NW India. J Geol Soc Ind 77:175–182

Singh T, Awasthi AK, Caputo R (2012) The sub-Himalayan fold-thrust belt in the 1905 Kangra earthquake zone: a critical taper model perspective for seismic hazard analysis. Tectonics 31:TC6002

Singh T, Awasthi AK, Kumar R, Virdi NS (2014) Drainage anomalies and absence of intermontane valleys characterize the outermost structural discontinuity and tectonic boundary in the Nahan Salient of Western Indian Sub-Himalaya. Geodyn Res Int Bull 1:26–33

Singh S, Awasthi AK, Khanna Y, Kumari A, Singh B, Kumar A, Popli C (2021) Sediment colour as recorder of climate and tectonics: cenozoic continental red beds of the Himalayan foreland basin in NW India. CATENA 203:105298

Sperner B, Zweigel P (2010) A plea for more caution in fault–slip analysis. Tectonophysics 482:29–41

Thakur M, Singh G, Malik JN (2021) Geological and geomorphic evidences of neotectonic activity along the Himalayan Frontal Thrust, Nahan Salient, NW Himalaya, India. Quat Int 575–576:5–20

Tranos MD (2017) The use of stress tensor discriminator faults in separating heterogeneous fault-slip data with best-fit stress inversion methods. J Struct Geol 102:168–178

Vaka DS, Rao YS, Singh T (2020) Surface Deformation of The 2019 Mirpur Earthquake Estimated from Sentinel-1 Insar Data. In: 2020 IEEE India geoscience and remote sensing symposium (InGARSS). IEEE, pp 130–133

Vanik N, Shaikh MA, Mukherjee S, Maurya DM, Chamyal LS (2018) Post-deccan trap stress reorientation under transpression: evidence from fault slip analysis from SW Saurashtra, Western India. J Geodyn 121:9–19

Walker RT (2006) A remote sensing study of active folding and faulting in southern Kerman province, SE Iran. J Struct Geol 28:654–668

Whipple KX, Tucker GE (1999) Dynamics of the stream-power river incision model: implications for height limits of mountain ranges, landscape response timescales, and research needs. J Geophys Res Solid Earth 104:17661–17674

Whittaker AC, Boulton SJ (2012) Tectonic and climatic controls on knickpoint retreat rates and landscape response times. J Geophys Res 117:F02024

Wobus C, Whipple KX, Kirby E, Snyder N, Johnson J, Spyropolou K, Crosby B, Sheehan D (2006) Tectonics from topography: procedures, promise, and pitfalls. In: Willett SD, Hovius N, Brandon MT, Fisher DM (eds) Tectonics, climate, and landscape evolution, vol 398. Geol Soc Am Spec Pap, pp 55–74

Yamaji A, Sato K (2019) Stress inversion meets plasticity theory: a review of the theories of fault-slip analysis from the perspective of the deviatoric stress-strain space. J Struct Geol 125:296–310

Žalohar J, Vrabec M (2008) Combined kinematic and paleostress analysis of fault-slip data: the multiple-slip method. J Struct Geol 30:1603–1613